Acta Materialia 171 (2019) 176–183

Contents lists available at ScienceDirect

Acta Materialia

journal homepage: www.elsevier.com/locate/actamat

Full length article

Evolution of flux-closure domain arrays in oxide multilayers with misfit strain

S. Li [a, b], Y.J. Wang [a], Y.L. Zhu [a, *], Y.L. Tang [a], Y. Liu [a], J.Y. Ma [a, b, c], M.J. Han [a, b], Bo Wu [a, d], X.L. Ma [a, c]

[a] Shenyang National Laboratory for Materials Science, Institute of Metal Research, Chinese Academy of Sciences, 72 Wenhua Road, 110016, Shenyang, China
[b] University of Chinese Academy of Sciences, 19 Yuquan Road, 100049, Beijing, China
[c] State Key Lab of Advanced Processing and Recycling on Non-ferrous Metals, Lanzhou University of Technology, Lanzhou, 730050, China
[d] School of Materials Science and Engineering, University of Science and Technology of China, Hefei, 230026, China

ARTICLE INFO

Article history:
Received 22 October 2018
Received in revised form
21 March 2019
Accepted 12 April 2019
Available online 15 April 2019

Keywords:
Ferroelectric film
Flux-closure domain
Misfit strain
Aberration corrected transmission electron microscope
Phase field modeling

ABSTRACT

Ferroelectric flux-closure domains have attracted great attention due to their potentials in high density data storage. For their future applications, it is important to understand their evolution with different factors, such as misfit strain. In this work, a flux-closure domain consisting of a vertical 180° domain wall with two symmetric *a* domains in both ends ("I" type closure) was observed in nearly unstrained $SrTiO_3$/$PbTiO_3$ multilayers by aberration corrected Transmission Electron Microscopy, which was speculated to be mainly induced by the strong depolarization field near the interface. With the tensile strain increasing, the small *a* domains in "I" type flux-closures grow gradually and eventually change to the well-known "V" type flux-closures. On the basis of a combination of experimental results and phase field simulations, the phase diagram of the stabilized domain arrays versus the strains in $PbTiO_3$ films are established. These results provide significant information on understanding the formation mechanism of flux-closure domains and shed light on their controlled growth. In addition, it paves a way to reduce the economic cost in their commercial applications because the $SrTiO_3$ substrate is easy to synthesize and much cheaper than scandate substrates.

© 2019 Acta Materialia Inc. Published by Elsevier Ltd. All rights reserved.

1. Introduction

The ability to synthesize heteroepitaxial complex oxides has enabled unprecedented access to manipulate degrees of freedom, while the lowering of symmetry provides a plethora of exotic physical phenomena [1–4]. Various peculiar phenomena and polar domain states have been predicted and observed in ferroelectric/dielectric heterostructure [5–8]. Among them, flux-closure domains and continuous topological states (so called vortex) in $SrTiO_3$/$PbTiO_3$ (STO/PTO) multilayers have attracted great attention due to their prospect in high density data storage [9–11]. Ferroelectric flux-closures are intriguing domain patterns characterized by closed head-to-tail continuous electric dipoles and they become vortices when the continuous rotation takes place around a vortex core, analogous to those in ferromagnetics [12–14]. With the experimental discoveries of long-range ordered flux-closure domain structures [10] and vortex arrays [11], researchers focus their interest on discovering flux-closures with new configuration, evaluating their formation conditions and understanding their evolution with external fields.

In 2015, Tang et al. reported the observation of periodic flux-closure arrays in PTO layers of STO/PTO multilayers grown on $GdScO_3$ (GSO) substrates. In the meantime, they found the dependence between the periodicity of flux-closure domains and the PTO layer thickness in the thickness range of 15–35 nm [10]. Subsequently, by further reducing the thickness of the PTO layer to about 4 nm, Yadav et al. observed polar vortex arrays in STO/PTO superlattices grown on $DyScO_3$ (DSO) substrates and their co-operators confirmed the phase evolution with one layer thickness by considering the counterbalance of electrostatic energy, elastic energy and polarization gradient-related interactions using phase field simulations [11,15]. Besides single layer thickness, the thickness ratio of adjacent PTO layers was found effective in manipulating the configurations of flux-closures [16]. This phenomenon is attributed to out-of-plane strain discontinuity and the phase

* Corresponding author.
E-mail address: ylzhu@imr.ac.cn (Y.L. Zhu).

https://doi.org/10.1016/j.actamat.2019.04.020
1359-6454/© 2019 Acta Materialia Inc. Published by Elsevier Ltd. All rights reserved.

diagram of the domain structure versus the thickness ratio was shown as a result of energy minimization. Besides the thickness, the effect of electric boundary condition on the evolution of flux-closures was also studied in our recent work, which is interpreted mainly by the changing of depolarization field [17]. By applying a range of characterization techniques and simulations, the vortex is considered to be a low-temperature stable phase and its interconversion with ferroelectric a_1/a_2 phase under the external electric field was investigated in detail very recently [18].

According to these works above, the tensile constrains provided by scandate substrates play an important role in the formation of flux-closure domains. Indeed, it is widely acknowledged that misfit strain shows remarkable ability to control domain patterns in epitaxial ferroelectric films [19–21]. Previously, the studies by X-ray scattering and atomic force microscopy showed that PTO thin films grown on STO (001) substrates tended to form period 180° stripe domains [22–24]. It is possible that the 180° domains may develop to flux-closure domains when sandwiched by STO layers because some pioneer works indicated that the strong depolarization field near the interface with insulating STO could cause the rotation of the local ferroelectric polarization [25–28]. In this work, the $(STO/PTO)_2$ multilayers were grown on STO(001), $DSO(110)_o$, and $GSO(110)_o$ substrates by pulsed laser deposition to investigate the effect of in-plane strain on flux-closure domain structures. The PTO film thickness is about 16 nm which is suitable for flux-closure domain formation and is also relatively thin to maintain strong depolarization field. The STO layer is used as an insulation interlayer and also to block the ambient screening charges at the surface which may influence the domain structure [29]. In the nearly unstrained multilayers on STO, we obtained flux-closure quadrant arrays with new morphologies (named "I" type), which consists of a 180° domain wall perpendicular to the interfaces with small *a* domains on two ends, demonstrating that the flux-closure domain could arise from the strong depolarization field and exist stably in nearly unstrained ferroelectric films. With the tensile strain increasing, the small *a* domains in "I" type closure became stressful and larger, while the domain configuration gradually changes to the known flux-closure domain with one large and one small *a* domains. Based on a combination of experimental result and phase field simulations, we establish the phase diagram of the stabilized domain arrays versus the strains in $PbTiO_3$ films, in which the bulk and elastic energies play dominated roles. These results provide significant information to understand the formation mechanism of flux-closure domains.

2. Experimental and simulational methods

The $(STO/PTO)_2$ multilayered films were deposited on STO(001), $DSO(110)_o$, $GSO(110)_o$ substrates by pulsed laser deposition, using a 248 nm KrF excimer laser. The PTO target was 3 mol% lead-enriched sintered ceramics while STO target was stoichiometric. Before deposition, the substrates were heated at 800 °C for 5 min and then kept at 700 °C. During the growth of PTO and STO, an oxygen pressure of 75 mTorr, a laser energy of 350 mJ and a repetition rate of 4 Hz were used. After growth, the film was stabilized at 700 °C for 5 min and then cooled down to room temperature at 5 °C/min in an oxygen pressure of 2×10^2 Torr. The cross-sectional samples for TEM and STEM observation were prepared by slicing, grinding, dimpling and finally ion milling by using Gatan PIPS.

Diffraction contrast TEM images were recorded using a Tecnai G^2 F30 transmission electron microscope (FEI). HAADF/ABF-STEM images were recorded using a Titan G^2 60-300 microscope with a high-brightness field-emission gun and double aberration (Cs) correctors from CEOS operating at 300 kV. Rotation mapping were deduced by using custom plugins of GPA for Gatan Digital Micrograph [30]. The atom column positions were determined by fitting them as 2D Gaussian peaks using Matlab software [31]. The displacement vector (δ_{Ti}) was calculated as a vector between each Ti^{4+} and the center of mass of its four nearest A-site neighbor Pb^{2+} and the noise for a specific unit cell was reduced by smoothing 9 unit cells around it.

The computation model consists of a $PbTiO_3$ (PTO) film, sandwiched by two $SrTiO_3$ (STO) layers, to simulate the insulated (open-circuit) boundary condition in the experiments. The size of the simulation box is $128 \times 128 \times 72$, corresponding to the real space size of $128 \times 128 \times 36\ nm^3$, where the thickness of the PTO film is 16 nm and the thicknesses of the two STO layer are both 10 nm. For the calculation of energy densities, only the PTO film is considered. The system energy is composed of bulk, gradient, elastic and electrostatic energies. The evolution of polarizations is simulated by the time-dependent Ginzburg-Landau equation: $dP_i/dt = -L \cdot \delta F/\delta P_i$. The corresponding energy functional formulae and the method to solve the equations have been described in many previous literature [16,32]. The bulk energy density coefficients of PTO and STO are adopted from previous literature [33,34]. We assume an interface region of one grid thickness exists between PTO and STO and the coefficients at these regions are the average value of PTO and STO. For the purpose of simplicity, all other material parameters of the whole system are taken as those of PTO, including the elastic constants, the dielectric constants and the electrostrictive coefficients [33].

3. Results and discussions

At room temperature, the bulk PTO is a tetragonal ferroelectric with the lattice parameters of $a = b = 3.90$ Å and $c = 4.15$ Å. According to the fact that the misfit dislocations may easily form in the PTO films under compressive strains in our previous experiments, the (pseudo)cubic (001) oriented perovskite oxide STO, DSO, and GSO single crystals with epitaxial strains ranging from 0.1% to 1.8% were chosen as substrates to insure the coherent growth without defects. The in-plane lattice misfits between the PTO films and substrates in the experimental and simulational conventions are comparatively shown in Table 1: the cubic lattice constant at Curie temperature (about 3.967 Å for PTO) is commonly used to get the misfit values in simulations instead of PTO's *a*-lattice parameter in experiments [35–37]. For simplicity, the strains represent for experimental values except for the phase field simulations.

Fig. 1 shows a $(STO/PTO)_2$ multilayer film grown on the STO substrate, in which the PTO layers are considered to be nearly unstrained. Fig. 1(a) is a cross-sectional dark field TEM image of the film, from which it can be seen that the interfaces of the film/substrate and PTO/STO are flat as denoted by the white arrow and white dash lines, respectively. Some stripe-like contrast fluctuations can be identified in the PTO layer indicating the existence of the domain pattern. It is obvious the domains in the upper PTO layer have a higher density and a homogeneous period compared with the lower layer. Since the lattice parameter of STO is very close to the *a*-lattice parameter of tetragonal PTO, *c* domains prefer to

Table 1
(Pseudo)cubic in-plane lattice parameters of the used substrates and in-plane lattice misfit with PTO in the experimental and simulational conventions.

		Misfit with $PbTiO_3$	
	a (Å)	Experiment	Simulation
$SrTiO_3$	3.905	0.1%	–1.6%
$DyScO_3$	3.950	1.3%	–0.4%
$GdScO_3$	3.969	1.8%	0.1%

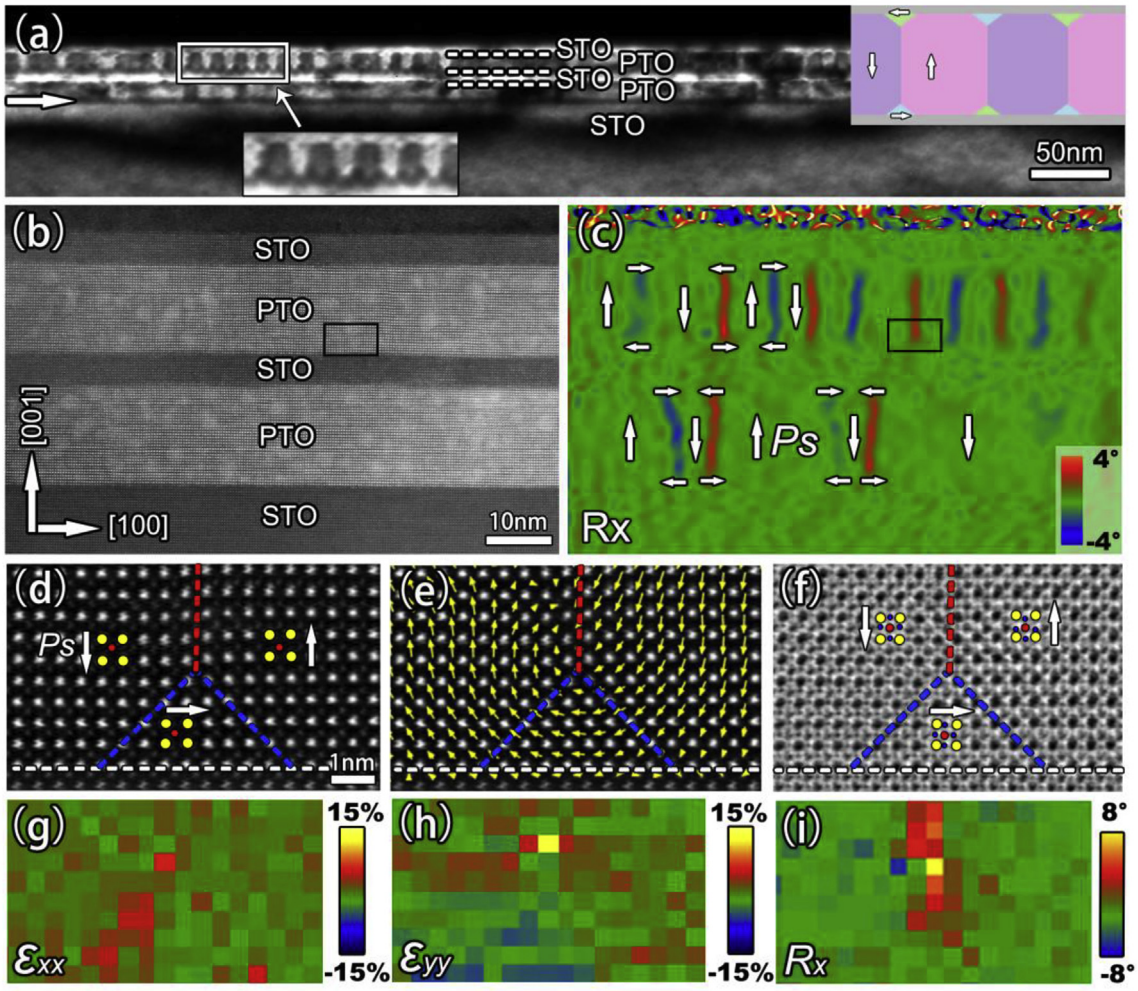

Fig. 1. "I" type flux-closure arrays in $(STO/PTO)_2$ multilayer films grown on STO substrates. (a) A cross-sectional dark field TEM image of the films, the left insert is an enlargement of white rectangle. The right insert is a sketch of the "I" type flux-closure arrays (the green, blue, pink, purple areas represent domains with different *Ps* orientations, as indicated by white arrows, while the gray area represents STO). (b, c) A high-resolution HAADF-STEM image and corresponding in-plane lattice rotation (R_x) mapping via GPA of the film. (d–f) Atomic-resolution HAADF-STEM image, Ti^{4+} ion displacement (δ_{Ti}) from Pb^{2+} lattice vectors mapping unit-cell by unit-cell and an ABF image of the areas labeled by the black rectangle in (b) and (c). (g–i) 2D mappings of in-plane strain (ε_{xx}), out-of-plane strain (ε_{yy}) and in-plane lattice rotation (R_x) of (d), respectively. The white arrows in (c, d, f) indicate the spontaneous polarization directions. The yellow, red and blue circles represent Pb, Ti and O atom columns, while the red, blue, white dash lines indicate 180°, 90° domain walls and the interface, respectively. The scheme of arrows, circles and lines is used in the following figures. (For interpretation of the references to colour in this figure legend, the reader is referred to the Web version of this article.)

form in the thin PTO film on STO. Due to the depolarization fields at the PTO/STO interfaces, the film contains some 180° domain walls between *c* domains with different polarization directions, which also have been reported before [22–24]. Therefore the contrast fluctuations in Fig. 1(a) are suspected to be the 180° domains. However, the zoom-in image shows a clearly bright and dark triangles at two ends of the 180° domain walls near the up and down interfaces, which indicates some domains with different polarization states exist here. On the basis of the vertex observed near the interface with insulator in previous studies [28,38], the triangle may represent a small *a* domain which can form a vertex with the neighbouring *c* domains. Meanwhile, it also implies a flux-closure domain exists there. The right insert in Fig. 1(a) is a sketch of this kind of flux-closure arrays, where the green, blue, pink, purple areas represent domains with different *Ps* orientations, as indicated by white arrows, while the gray area represents STO. In order to confirm this deduction, a high-resolution HAADF-STEM image and the corresponding in-plane rotation (R_x) mapping via geometric phase analysis (GPA) are shown in Fig. 1(b and c). The PTO layers are brighter than the STO layers because the atomic number of Pb is larger than that of Sr. It is noted that 180° domain walls in PTO layers are revealed as red and blue lines in Fig. 1(c) with their characteristics in lattice rotation. It was previously reported that there is a specific relationship between the lattice rotation and the spontaneous polarization (*Ps*) at 180° domain walls [39]. The *Ps* directions besides 180° domain walls can be identified according to the inhomogeneous rotations in Fig. 1(c), which are denoted by white arrows. While, based on the principle that the uncharged domain wall is more stable, the small white arrows represent the possible *Ps* directions of the small *a* domains which is unobservable in Fig. 1(c). To further verify the small *a* domain and flux-closure domain, the atomic-resolution HAADF-STEM image and the corresponding δ_{Ti} vectors (Ti^{4+} displacement from the center of the Pb^{2+} sublattice) mapping of the area labeled by the black rectangle in Fig. 1(b and c) are shown in Fig. 1(d and e). In Fig. 1(d), the yellow and red circles denote the positions of Pb and Ti atom columns, respectively. By spotting the positions of Pb and Ti atom columns, the *Ps* directions of each domain can be determined and denoted by

white arrows since it is opposite to the δ_{Ti} vector. The yellow arrows in Fig. 1(e) denote the δ_{Ti} vectors of unit cells, where a vertex with a small *a* domain can be observed clearly. The ABF image is shown in Fig. 1(f) to confirm the *Ps* directions directly from the asymmetry of positive and negative ion centers because the O atom columns (denoted by blue circles) are visible here. The red, blue and white dash lines indicate the 180°, 90° domain walls and interfaces, respectively, in Fig. 1(d–c) as well as in the following images. Combining the above results and discussions, the domain structures are identified as flux-closure arrays of two small *a* domains at each end of the 180° domain walls near the interface. For simplicity, this flux-closure domain is named "I" type closure.

To study the structural details, Fig. 1(g–i) show the in-plane strain (ε_{xx}), out-of-plane strain (ε_{yy}) and in-plane lattice rotation (R_x) mapping unit-cell by unit-cell of Fig. 1(d), respectively, which were obtained through peak finding. Compared with the *c* domains, the small *a* domain displays a slight increase of in-plane strain and a slight decrease of out-of-plane strain, while the in-plane rotation is barely to see in both Fig. 1(c) and (i). Considering the strong depolarization field may induce *Ps* rotation and the vertex formation [25,26,28], we speculate the small *a* domains here as a result of the strong depolarization field in PTO layers near the interface. Therefore, this *a* domain under substrate constraints is unable to maintain the lattice parameters of bulk and the rotation characteristic of 90° domain walls, which is consistent with our experimental results. As to the difference between domain patterns in upper and lower PTO layers in Fig. 1(a), it may be in connection with the different properties of STO substrates and the deposited STO, which may affect the depolarization field and then the domain configuration, since some previous works indicated the property of STO can be altered by growth conditions, such as the laser energy and the oxygen pressure [40,41].

A $(STO/PTO)_2$ multilayer film grown on the DSO substrate providing a middle tensile strain (1.3%) was shown in Fig. 2. From the cross-sectional dark field TEM image of the film (Fig. 2(a)), it is obvious that different domain structures exist in the upper and lower PTO layers. The lower layer shows sideling stripe contrasts which may be the typical *a*/*c* domain structures. The *a*/*c* domains seem to have the same domain wall direction, which implies there is a preferred polarization direction in *c* domains. This phenomenon may be connected to the asymmetric boundary condition in the lower layer, as discussed in our previous work [17]. As to the upper layer, there are two kinds of contrast distributions. One is vertical strips in the middle area, which seems to be the same structure in Fig. 1. The other is one-dimensional periodic sinusoidal arrays which is similar to the alternate clockwise and counterclockwise flux-closure quadrants named "V" type closure in multilayer PTO/STO films reported previously [10,16,17]. The insert in Fig. 2(a) shows a sketch of the domain arrays in the upper PTO layers. In order to confirm the domain patterns, a high-resolution HAADF-STEM image and the corresponding in-plane rotation (R_x) mapping via GPA of a characteristic region are shown in Fig. 2(b and c). According to the in-plane strain (not shown here) and rotation maps, the domain structure in the lower PTO layer is small *a* domains embedded in large *c* domains. The *Ps* directions in the upper PTO layer can be uniquely identified due to the 180° domain walls here with the method mentioned above. Therefore, the "I" type flux-closures as well as "V" type ones can be clearly observed in the upper layer, which verifies the speculations above. Since the "V" type closure has been studied carefully previously, so we focus on the structure details of the "I" type closure. Fig. 2(d–f) show an atomic-resolution HAADF-STEM image, the corresponding δ_{Ti} vector mapping and an ABF image of the area labeled by the black rectangle in Fig. 2(b and c). The *Ps* distributions of the vertex are in accord with the white arrows in Fig. 1(c). In contrast to the *a* domain in Fig. 1(d–f), the *a* domain here seems a little larger with more obvious rotation characteristic. To further compare the "I" type closures on STO and DSO, the in-plane strain (ε_{xx}), out-of-plane strain (ε_{yy}) and in-plane lattice rotation (R_x) mappings unit-cell by unit-cell of Fig. 2(d) are shown in Fig. 2(g–i), respectively. Compared with Fig. 1(g–i) with the same scale, the *a* domain of "I" type closure on DSO is more strained and the rotation near the 90° domain wall is closer to the normal value. It is believed this change is concerned with the tensile strain provided by DSO, which is beneficial to *a* domain formation and then induces the "V" type closure to form in the upper layer.

Along with the increase of the tensile strain, Fig. 3 shows a $(STO/PTO)_2$ multilayer film grown on a GSO substrate. Fig. 3(a) shows a cross-sectional dark field TEM image of the film, from which it is obvious that periodic "V" type closure arrays exist in the upper and lower layers. The insert is a sketch of the "V" type closure arrays with white arrows indicating the *Ps* direction. It is also in accordance with the experimental results in previous works [10,17]. A high-resolution HAADF-STEM image and the corresponding in-plane rotation (R_x) mapping via GPA of the film are shown in Fig. 3(b and c). The *Ps* directions are also denoted by white arrows. Considering the domain configurations in PTO layers on STO, DSO and GSO, the primary formation reasons of the big and small *a* domains in "V" type closure domains seem different. The small one is similar to these in "I" type closure whose major inducing factor is speculated as the strong depolarization field. However, the big one is mainly to balance the large tensile strain.

To explain the experimental results, phase field simulations were performed to study the evolution of domain structures with the epitaxial strain in the PTO film under the insulated boundary condition. Firstly, we chose the three strain states corresponding to the three substrates used in our experiments. The simulated domain structures are shown in Fig. 4. In the STO case (Fig. 4(a and b)), only "I" type closure domains were observed. From the polarization vector diagrams in Fig. 4(b), it is estimated that the sizes of *a* domains are about 2 nm in the *z* direction. In the DSO case (Fig. 4(c) and (e)), both "I" and "V" type closure domains were observed. In the GSO case (Fig. 4(d) and (f)), "V" type closure domains and a_1/a_2 domains were found to coexist. Comparing Fig. 4 with Figs. 1–3, it was found that the simulational and experimental results perfectly matched with each other for the cases of STO and DSO. For the GSO case, the coexistence of flux-closure and a_1/a_2 domains was observed in the plane-view samples, as shown in Fig. S1 in the supporting information. The cross-section image shown in Fig. 3 might incidentally capture the section of flux-closure domains. To sum up, all three simulation results were consistent with experimental findings.

From Fig. 4(b, e), the orientations of 180° domain walls seem random and display the labyrinthine domain structures. The reason may be that the gradient coefficient tensor used in our phase field simulations is isotropic. As a result, the 180° domain walls can be in any orientation. It is also noted that the labyrinthine domain structures have been predicted to form in ferroelectric nanoparticles due to the combined effect of the gradient coefficient and the surface screening length [42,43].

To further understand the effect of strain on the flux-closure domain structures, the domain fractions and energy densities of the PTO film were analyzed, trying to construct the phase diagram. The domain structures under different misfit strains are shown in Fig. 5. It is found that at large compressive strains, *c* domains with opposite polarizations dominate. However, small *a* domains exist at the intersections between the 180° domain walls and the interfaces, even for the largest compressive strain considered. With the decrease of compressive strain, the small *a* domains at the ends of 180° domain walls gradually enlarge. From the compressive

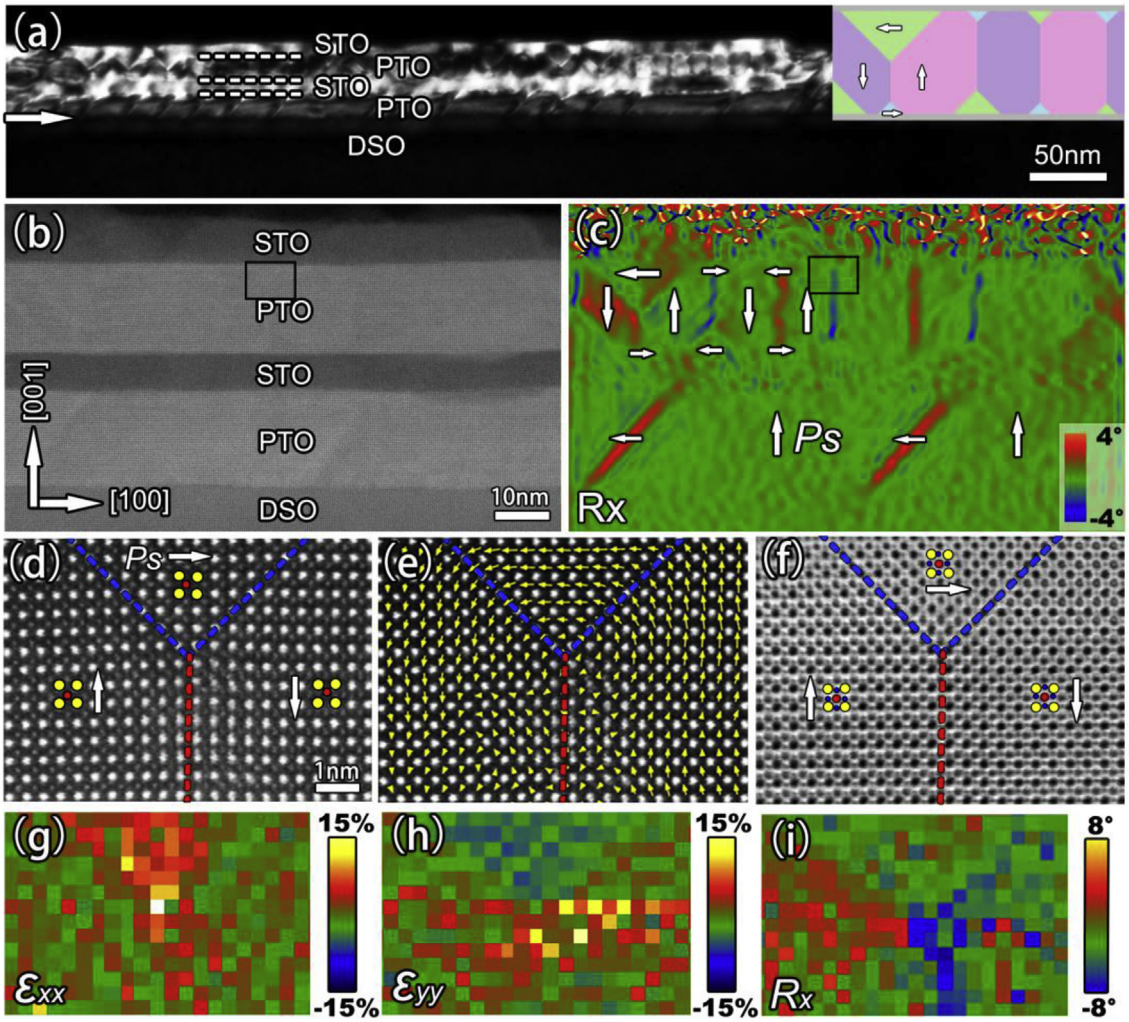

Fig. 2. "I" and "V" types flux-closure arrays in $(STO/PTO)_2$ multilayer films grown on DSO substrates. A cross-sectional dark field TEM image (a), a high-resolution HAADF-STEM image (b) and corresponding in-plane lattice rotation (R_x) mapping via GPA (c) of the film. The insert in (a) is a sketch of the "I" and "V" type flux-closure arrays (the green, blue, pink, purple areas represent domains with different *Ps* orientations, as indicated by white arrows, while the gray area represents STO). (d–f) Atomic-resolution HAADF-STEM image, Ti^{4+} ion displacement (δ_{Ti}) from Pb^{2+} sublattice mapping unit-cell by unit-cell and an ABF image of the areas labeled by the black rectangle in (b) and (c). (g–h) 2D mappings of in-plane strain (ε_{xx}), out-of-plane strain (ε_{yy}) and in-plane lattice rotation (R_x) of (d), respectively. (For interpretation of the references to colour in this figure legend, the reader is referred to the Web version of this article.)

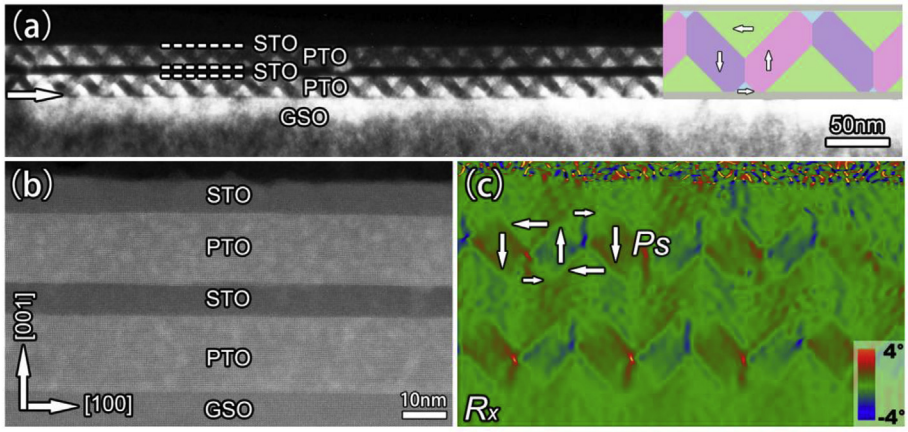

Fig. 3. "V" type flux-closure arrays in $(STO/PTO)_2$ multilayer films grown on the GSO substrates. A cross-sectional dark field TEM image (a), a high-resolution HAADF-STEM image (b) and corresponding in-plane lattice rotation (R_x) mapping via GPA (c) of the film. The right insert is a sketch of the "V" type flux-closure arrays (the green, blue, pink, purple areas represent domains with different *Ps* orientations, as indicated by white arrows, while the gray area represents STO). (For interpretation of the references to colour in this figure legend, the reader is referred to the Web version of this article.)

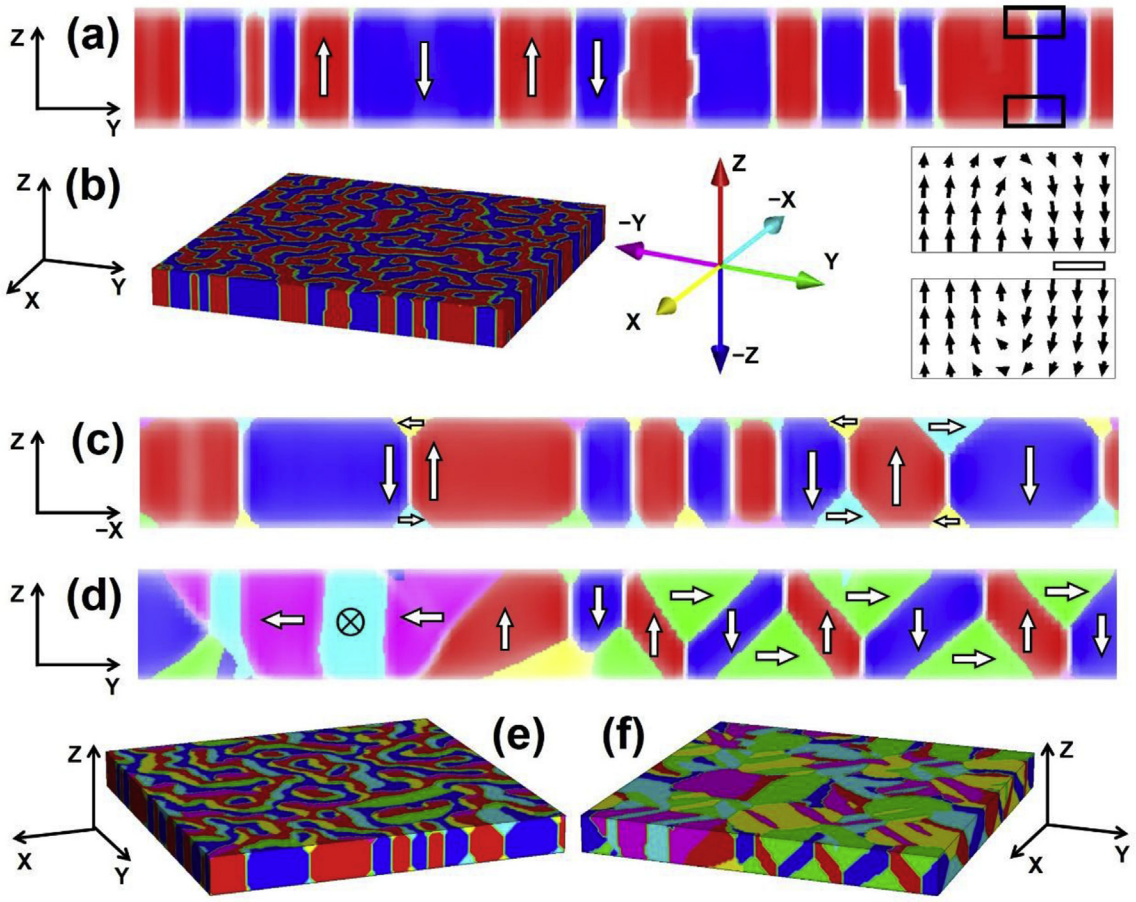

Fig. 4. The phase field simulation results of a 16 nm PTO film at different strain states under the open-circuit boundary condition. (a) and (b): on the STO substrate; (c) and (e): on the DSO substrate; (d) and (f): on the GSO substrate. The polarization vector diagrams in (b) are the zoom-in images of the black boxes in (a). The bar beside the vector diagrams indicate 2 nm.

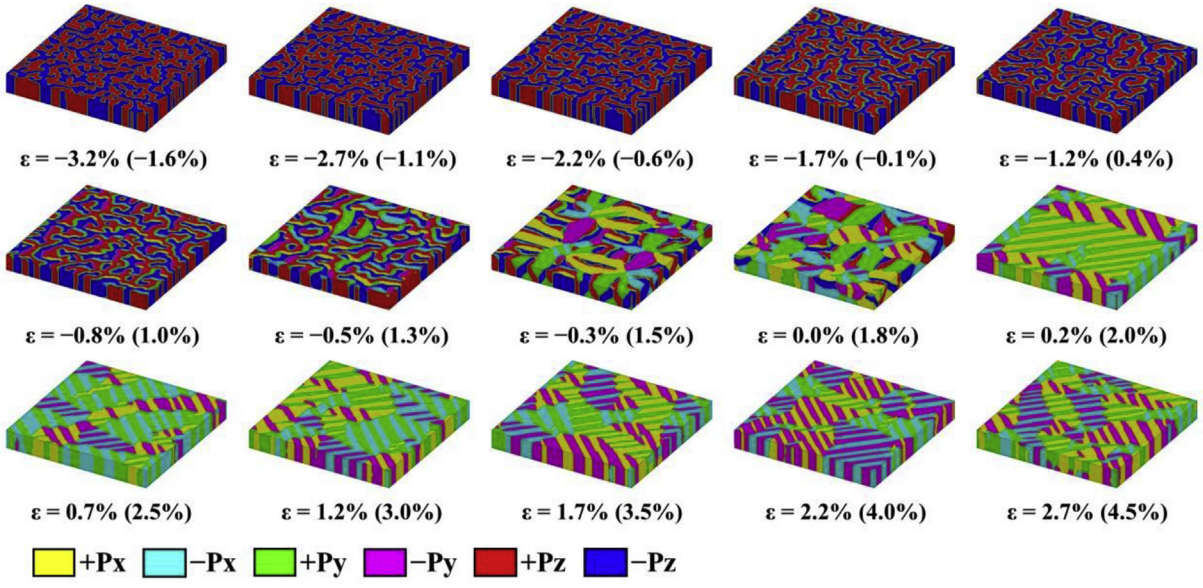

Fig. 5. The evolution of domain structure of the PTO film at different strain states. The strain values in the parentheses are in the experimental convention.

strain to the tensile one, the domain structure evolves from "I" type to "V" type flux-closure domains and finally a_1/a_2 domains.

To clearly reveal the transition of these domain structures, the fractions of the three domain structures are calculated, as shown in Fig. 6(a). The experimental and simulational misfit strains are comparatively shown at the top and bottom of Fig. 6. It is found that if the misfit strain is smaller than −0.5% (or 1.2% in the experimental convention), "I" type flux-closure domains dominate. For the strain state larger than 0.2% (or 1.9% in the experimental convention), a_1/a_2 domains dominate. In the intermediate range, "I" and "V" type flux-closure domains and a_1/a_2 domains coexist. The evolution of the total energy density with respect to strain is shown in Fig. 6(b). It is found that the total energy density shows a spinodal behavior, similar to previous studies [18,44,45]. The total energy density at each strain state is decomposed into those of the three types of domains, as also shown in Fig. 6(b). It is found that the total energy densities of the two types of flux-closure domains are very close to each other in the strain range between −0.5% and 0.0%, and around the strain state of −0.2%, all the three domains possess nearly the same total energy densities. That explains the coexistence of the three type domain structures. It is well known that the formation of domain structures in ferroelectric films is the competition between a series of energies, including the bulk, gradient, elastic and electrostatic energies. The evolutions of different energy densities with strain are shown in Fig. S2. It is found that the electrostatic energy is large in the flux-closure region and almost zero in the a_1/a_2 region, which testify the above supposition that the depolarization field plays an important role in the formation of *a* domains in flux-closure domains. It is also found that only the bulk and elastic energy densities show the spinodal behavior, which indicates that these two energies dominate at the transition from flux-closure to a_1/a_2 domains.

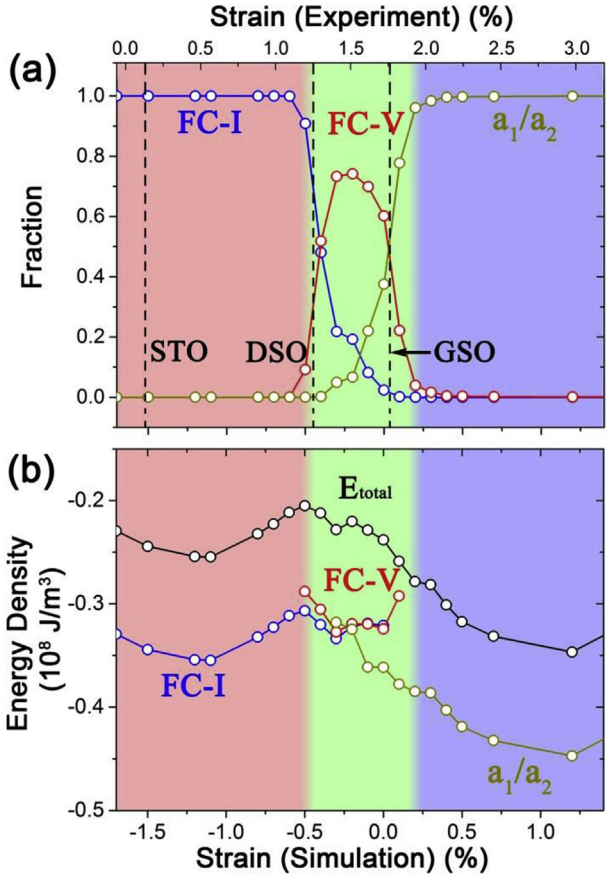

Fig. 6. Phase diagram of a 16 nm PTO film at different strain states under the open-circuit boundary condition obtained by phase field simulations. (a) The fractions of "I" and "V" type flux-closures and a_1/a_2 domains. (b) The energy density of the PTO film. The black circles are the total energy density; the blue, red and dark yellow ones are the total energy densities of "I" and "V" type flux-closures and a_1/a_2 domains. To distinguish the total and partial energy densities, the curve of the total energy density is shifted upward by 0.1×10^8 J/m^3. The strain values in the experimental and simulational conventions are comparatively shown at the top and bottom of the figure. To clearly reveal the transition region, only part of the strain range is shown. (For interpretation of the references to colour in this figure legend, the reader is referred to the Web version of this article.)

4. Conclusion

In summary, we analyzed the evolution of flux-closure domain configurations in $SrTiO_3/PbTiO_3$ multilayers with strains by aberration corrected Transmission Electron Microscopy and phase field simulations. A flux-closure domain named "I" type consisting of a vertical 180° domain wall with two small and symmetric *a* domains was observed in nearly unstrained multilayers, which was speculated to be mainly induced by the strong depolarization field near the interfaces. The results of experiments and phase field simulations both show the small *a* domains in "I" type closure begin to grow and gradually change to the known "V" type closure with one large and one small *a* domains as the tensile strain increases. We also established the phase diagram of the stabilized domain arrays versus the strains for the $PbTiO_3$ film. These results provide significant information to understand the formation mechanism of flux-closure and also help reduce the economic cost in its commercial applications because the $SrTiO_3$ substrate is easier to synthesize and cheaper than scandate substrates.

Acknowledgement

This work is supported by the National Natural Science Foundation of China (Nos. 51571197, 51501194, 51671194), National Basic Research Program of China (2014CB921002), and the Key Research Program of Frontier Sciences CAS (QYZDJ-SSW-JSC010). Y.L.T. acknowledges the IMR SYNL-T.S. Kê Research Fellowship and the Youth Innovation Promotion Association CAS (No. 2016177).

Appendix A. Supplementary data

Supplementary data to this article can be found online at https://doi.org/10.1016/j.actamat.2019.04.020.

References

[1] A. Ohtomo, H.Y. Hwang, A high-mobility electron gas at the $LaAlO_3/SrTiO_3$ heterointerface, Nature 427 (6973) (2004) 423–426.
[2] H.N. Lee, H.M. Christen, M.F. Chisholm, C.M. Rouleau, D.H. Lowndes, Strong polarization enhancement in asymmetric three-component ferroelectric superlattices, Nature 433 (7024) (2005) 395–399.
[3] J. Mannhart, D.G. Schlom, Oxide interfaces—an opportunity for electronics, Science 327 (5973) (2010) 1607–1611.
[4] P. Zubko, S. Gariglio, M. Gabay, P. Ghosez, J.-M. Triscone, Interface physics in complex oxide heterostructures, in: Annual Review of Condensed Matter Physics, vol. 2, 2011, pp. 141–165.
[5] J. Kim, Y. Kim, Y.S. Kim, J. Lee, L. Kim, D. Jung, Large nonlinear dielectric properties of artificial $BaTiO_3/SrTiO_3$ superlattices, Appl. Phys. Lett. 80 (19) (2002) 3581–3583.
[6] P. Aguado-Puente, J. Junquera, Structural and energetic properties of domains in $PbTiO_3/SrTiO_3$ superlattices from first principles, Phys. Rev. B 85 (18) (2012) 184105.
[7] P. Zubko, N. Jecklin, N. Stucki, C. Lichtensteiger, G. Rispens, J.M. Triscone, Ferroelectric domains in $PbTiO_3/SrTiO_3$ superlattices, Ferroelectrics 433 (2012) 127–137.
[8] J.Y. Jo, P. Chen, R.J. Sichel, S.J. Callori, J. Sinsheimer, E.M. Dufresne, M. Dawber, P.G. Evans, Nanosecond dynamics of ferroelectric/dielectric superlattices, Phys. Rev. Lett. 107 (5) (2011) 055501.
[9] Naumov II, L. Bellaiche, H.X. Fu, Unusual phase transitions in ferroelectric

nanodisks and nanorods, Nature 432 (7018) (2004) 737–740.
[10] Y.L. Tang, Y.L. Zhu, X.L. Ma, A.Y. Borisevich, A.N. Morozovska, E.A. Eliseev, W.Y. Wang, Y.J. Wang, Y.B. Xu, Z.D. Zhang, S.J. Pennycook, Observation of a periodic array of flux-closure quadrants in strained ferroelectric $PbTiO_3$ films, Science 348 (6234) (2015) 547–551.
[11] A.K. Yadav, C.T. Nelson, S.L. Hsu, Z. Hong, J.D. Clarkson, C.M. Schlepueetz, A.R. Damodaran, P. Shafer, E. Arenholz, L.R. Dedon, D. Chen, A. Vishwanath, A.M. Minor, L.Q. Chen, J.F. Scott, L.W. Martin, R. Ramesh, Observation of polar vortices in oxide superlattices, Nature 530 (7589) (2016) 198–201.
[12] D.J. Srolovitz, J.F. Scott, Clock-model description of incommensurate ferroelectric-films and of nematic-liquid-crystal films, Phys. Rev. B 34 (3) (1986) 1815–1819.
[13] A. Schilling, D. Byrne, G. Catalan, K.G. Webber, Y.A. Genenko, G.S. Wu, J.F. Scott, J.M. Gregg, Domains in ferroelectric nanodots, Nano Lett. 9 (9) (2009) 3359–3364.
[14] T. Shinjo, T. Okuno, R. Hassdorf, K. Shigeto, T. Ono, Magnetic vortex core observation in circular dots of permalloy, Science 289 (5481) (2000) 930–932.
[15] Z. Hong, A.R. Damodaran, F. Xue, S.-L. Hsu, J. Britson, A.K. Yadav, C.T. Nelson, J.J. Wang, J.F. Scott, L.W. Martin, R. Ramesh, L.Q. Chen, Stability of polar vortex lattice in ferroelectric superlattices, Nano Lett. 17 (4) (2017) 2246–2252.
[16] Y. Liu, Y.J. Wang, Y.L. Zhu, C.H. Lei, Y.L. Tang, S. Li, S.R. Zhang, J. Li, X.L. Ma, Large scale two-dimensional flux-closure domain arrays in oxide multilayers and their controlled growth, Nano Lett. 17 (12) (2017) 7258–7266.
[17] S. Li, Y.L. Zhu, Y.J. Wang, Y.L. Tang, Y. Liu, S.R. Zhang, J.Y. Ma, X.L. Ma, Periodic arrays of flux-closure domains in ferroelectric thin films with oxide electrodes, Appl. Phys. Lett. 111 (5) (2017).
[18] A.R. Damodaran, J.D. Clarkson, Z. Hong, H. Liu, A.K. Yadav, C.T. Nelson, S.L. Hsu, M.R. McCarter, K.D. Park, V. Kravtsov, A. Farhan, Y. Dong, Z. Cai, H. Zhou, P. Aguado-Puente, P. García-Fernández, J. Íñiguez, J. Junquera, A. Scholl, M.B. Raschke, L.Q. Chen, D.D. Fong, R. Ramesh, L.W. Martin, Phase coexistence and electric-field control of toroidal order in oxide superlattices, Nat. Mater. 16 (2017) 1003.
[19] D.G. Schlom, L.Q. Chen, C.J. Fennie, V. Gopalan, D.A. Muller, X. Pan, R. Ramesh, R. Uecker, Elastic strain engineering of ferroic oxides, MRS Bull. 39 (02) (2014) 118–130.
[20] Y.L. Li, S.Y. Hu, Z.K. Liu, L.Q. Chen, Phase-field model of domain structures in ferroelectric thin films, Appl. Phys. Lett. 78 (24) (2001) 3878–3880.
[21] F. Borodavka, I. Gregora, A. Bartasyte, S. Margueron, V. Plausinaitiene, A. Abrutis, J. Hlinka, Ferroelectric nanodomains in epitaxial $PbTiO_3$ films grown on $SmScO_3$ and $TbScO_3$ substrates, J. Appl. Phys. 113 (18) (2013) 187216.
[22] S.K. Streiffer, J.A. Eastman, D.D. Fong, C. Thompson, A. Munkholm, M.V.R. Murty, O. Auciello, G.R. Bai, G.B. Stephenson, Observation of nanoscale 180 degrees stripe domains in ferroelectric $PbTiO_3$ thin films, Phys. Rev. Lett. 89 (6) (2002) 067601.
[23] D.D. Fong, G.B. Stephenson, S.K. Streiffer, J.A. Eastman, O. Auciello, P.H. Fuoss, C. Thompson, Ferroelectricity in ultrathin perovskite films, Science 304 (5677) (2004) 1650–1653.
[24] C. Thompson, D.D. Fong, R.V. Wang, F. Jiang, S.K. Streiffer, K. Latifi, J.A. Eastman, P.H. Fuoss, G.B. Stephenson, Imaging and alignment of nanoscale 180° stripe domains in ferroelectric thin films, Appl. Phys. Lett. 93 (18) (2008) 182901.
[25] P. Zubko, N. Jecklin, A. Torres-Pardo, P. Aguado-Puente, A. Gloter, C. Lichtensteiger, J. Junquera, O. Stephan, J.M. Triscone, Electrostatic coupling and local structural distortions at interfaces in ferroelectric/paraelectric superlattices, Nano Lett. 12 (6) (2012) 2846–2851.
[26] G.Y. Kim, K. Chu, K.D. Sung, H.S. Lee, S.D. Kim, K. Song, T. Choi, J. Lee, J.P. Buban, S.Y. Yoon, K.H. Kim, C.H. Yang, S.Y. Choi, Disordered ferroelectricity in the $PbTiO_3/SrTiO_3$ superlattice thin film, Apl. Mater. 5 (6) (2017) 066104.
[27] Z.D. Zhou, D.Y. Wu, Domain structures of ferroelectric films under different electrical boundary conditions, AIP Adv. 5 (10) (2015) 107206.
[28] C.L. Jia, K.W. Urban, M. Alexe, D. Hesse, I. Vrejoiu, Direct observation of continuous electric dipole rotation in flux-closure domains in ferroelectric $Pb(Zr,Ti)O_3$, Science 331 (6023) (2011) 1420–1423.
[29] I.S. Vorotiahin, E.A. Eliseev, Q. Li, S.V. Kalinin, Y.A. Genenko, A.N. Morozovska, Tuning the polar states of ferroelectric films via surface charges and flexoelectricity, Acta Mater. 137 (2017) 85–92.
[30] M.J. Hytch, E. Snoeck, R. Kilaas, Quantitative measurement of displacement and strain fields from HREM micrographs, Ultramicroscopy 74 (3) (1998) 131–146.
[31] S.M. Anthony, S. Granick, Image analysis with rapid and accurate two-dimensional Gaussian fitting, Langmuir 25 (14) (2009) 8152–8160.
[32] Y.J. Wang, J. Li, Y.L. Zhu, X.L. Ma, Phase-field modeling and electronic structural analysis of flexoelectric effect at 180° domain walls in ferroelectric $PbTiO_3$, J. Appl. Phys. 122 (22) (2017) 224101.
[33] Y.L. Li, S.Y. Hu, Z.K. Liu, L.Q. Chen, Effect of substrate constraint on the stability and evolution of ferroelectric domain structures in thin films, Acta Mater. 50 (2) (2002) 395–411.
[34] Y.L. Li, S.Y. Hu, D. Tenne, A. Soukiassian, D.G. Schlom, X.X. Xi, K.J. Choi, C.B. Eom, A. Saxena, T. Lookman, Q.X. Jia, L.Q. Chen, Prediction of ferroelectricity in $BaTiO_3/SrTiO_3$ superlattices with domains, Appl. Phys. Lett. 91 (11) (2007) 112914.
[35] Y.Y. Liu, Z.X. Zhu, J.F. Li, J.Y. Li, Misfit strain modulated phase structures of epitaxial $Pb(Zr_{1-x}Ti_x)O_3$ thin films: the effect of substrate and film thickness, Mech. Mater. 42 (8) (2010) 816–826.
[36] Y.Y. Liu, J.Y. Li, Shear-driven morphotropic phase boundary in epitaxial ferroelectric thin films, Phys. Rev. B 84 (13) (2011) 132104.
[37] M.J. Haun, E. Furman, S.J. Jang, H.A. McKinstry, L.E. Cross, Thermodynamic theory of $PbTiO_3$, J. Appl. Phys. 62 (8) (1987) 3331–3338.
[38] C.T. Nelson, B. Winchester, Y. Zhang, S.J. Kim, A. Melville, C. Adamo, C.M. Folkman, S.H. Baek, C.B. Eom, D.G. Schlom, L.Q. Chen, X. Pan, Spontaneous vortex nanodomain arrays at ferroelectric heterointerfaces, Nano Lett. 11 (2) (2011) 828–834.
[39] Y.L. Tang, Y.L. Zhu, X.L. Man, On the benefit of aberration-corrected HAADF-STEM for strain determination and its application to tailoring ferroelectric domain patterns, Ultramicroscopy 160 (2016) 57–63.
[40] G.Z. Liu, Q.Y. Lei, X.X. Xi, Stoichiometry of $SrTiO_3$ films grown by pulsed laser deposition, Appl. Phys. Lett. 100 (20) (2012) 202902.
[41] T. Ohnishi, M. Lippmaa, T. Yamamoto, S. Meguro, H. Koinuma, Improved stoichiometry and misfit control in perovskite thin film formation at a critical fluence by pulsed laser deposition, Appl. Phys. Lett. 87 (24) (2005) 241919.
[42] A.N. Morozovska, Y.M. Fomichov, P. Maksymovych, Y.M. Vysochanskii, E.A. Eliseev, Analytical description of domain morphology and phase diagrams of ferroelectric nanoparticles, Acta Mater. 160 (2018) 109–120.
[43] E.A. Eliseev, Y.M. Fomichov, S.V. Kalinin, Y.M. Vysochanskii, P. Maksymovich, A.N. Morozovska, Labyrinthine domains in ferroelectric nanoparticles: manifestation of a gradient-induced morphological transition, Phys. Rev. B 98 (5) (2018) 054101.
[44] F. Xue, Y. Li, Y. Gu, J. Zhang, L.-Q. Chen, Strain phase separation: formation of ferroelastic domain structures, Phys. Rev. B 94 (22) (2016) 220101.
[45] A.R. Damodaran, S. Pandya, J.C. Agar, Y. Cao, R.K. Vasudevan, R. Xu, S. Saremi, Q. Li, J. Kim, M.R. McCarter, L.R. Dedon, T. Angsten, N. Balke, S. Jesse, M. Asta, S.V. Kalinin, L.W. Martin, Three-state ferroelastic switching and large electromechanical responses in $PbTiO_3$ thin films, Adv. Mater. 29 (37) (2017) 1702069.